

Real-time GW -Ehrenfest-Fan-Migdal method for nonequilibrium 2D materials

Enrico Perfetto^{*,†,‡} and Gianluca Stefanucci^{†,‡}

[†]*Dipartimento di Fisica, Università di Roma Tor Vergata, Via della Ricerca Scientifica 1,
00133 Rome, Italy*

[‡]*INFN, Sezione di Roma Tor Vergata, Via della Ricerca Scientifica 1, 00133 Rome, Italy*

E-mail: enrico.perfetto@roma2.infn.it

Abstract

Quantum simulations of photoexcited low-dimensional systems are pivotal for understanding how to functionalize and integrate novel two-dimensional (2D) materials in next-generation optoelectronic devices. First principles predictions are extremely challenging due to the simultaneous interplay of light-matter, electron-electron and electron-nuclear interactions. We here present an advanced ab initio many-body method which accounts for quantum coherence and non-Markovian effects while treating electrons and nuclei on equal footing, thereby preserving fundamental conservation laws like the total energy. The impact of this advancement is demonstrated through real-time simulations of the complex multivalley dynamics in a molybdenum disulfide (MoS_2) monolayer pumped above gap. Within a single framework we provide a parameter-free description of the coherent-to-incoherent crossover, elucidating the role of microscopic and collective excitations in the dephasing and thermalization processes.

1 Introduction

The ultrafast electronic, transport and optical properties of semiconductors are determined by their response to a photoexcitation. Understanding the underlying microscopic dynamics is crucial for technological applications in

optoelectronics,^{1–4} photovoltaics^{5–7} and photocatalysis.^{8–10} The number of experimental time-resolved studies in advanced materials like transition metal dichalcogenides (TMD) has virtually exploded over the last ten years.^{11–14} The emerging universal picture is that the quantum dynamics initiated by an ultrafast excitation is characterized by two distinct and consecutive regimes: an initially coherent regime featuring a macroscopic polarization that oscillates on the femtoseconds time-scale and a subsequent incoherent (or depolarized) regime during which the excited carriers bring to completion the thermalization and then cool down.¹⁵ A unified theoretical framework capable of simulating the real-time dynamics from the coherent to the incoherent regime would be utmost desirable for parameter-free predictions.

The challenge is to simultaneously account for material-specific ab initio electronic and phononic band structures, light-matter, electron-electron (*el-el*) and electron-phonon (*el-ph*) interactions. Methods like Time-Dependent Density-Functional Theory^{16–18} in the typical adiabatic flavour^{19,20} or time-dependent GW Bethe-Salpeter^{21,22} account for both polarization and carrier dynamics but are limited to the coherent kinetics as correlation-induced dephasing mechanisms (responsible for the damping of the polarization) and relaxation processes (responsible for thermalization and cooling) are missing. Approaches based on the Boltzmann Equation (BE)^{23,24} treat relax-

ation processes at a Markovian level and are therefore suited to simulate thermalization and cooling (incoherent regime). In fact, BE has no access to the coherent dynamics since the polarization is assumed to vanish from the outset. The microscopic description of the coherent-to-incoherent crossover has therefore remained elusive so far. In the coherent regime scattering processes are intrinsically time-nonlocal and it is precisely such non-locality that is necessary to capture the correlation-induced dephasing.²⁴ State-of-the-art methods based on the more advanced semiconductor Bloch equations^{25,26} treat the polarization degrees of freedom semiclassically and ignore their feedback on the carrier dynamics,^{27–29} thus violating the conservation of the total energy. Another difficult aspect of the crossover is that for laser pulses shorter than the screening buildup time the effective interaction between hot carriers is neither the bare Coulomb interaction nor the fully developed screened one.^{26,30} Addressing all this physics calls for a non-Markovian treatment of electronic and phononic correlations within a framework that handles polarization and carrier degrees-of-freedom on equal footing. In this work we provide a versatile ab initio method based on nonequilibrium Green's function (NEGF)³¹ which encompasses all required features.

We build on a recent time-linear scheme^{32–35} based on the Generalized Kadanoff-Baym Ansatz for electrons³⁶ and phonons³⁷ to solve the NEGF equations for the nonequilibrium electronic *and* phononic density matrices. We pioneer the simultaneous inclusion of *el-el* correlations at the *GW* level³⁸ and *el-ph* correlations at the Ehrenfest plus Fan-Migdal (FM) level.³⁷ No further approximations like time-local screening or frozen phonons are introduced; the polarization decays without any phenomenological or semi-empirical dephasing rate. Simulations up to hundreds of femtoseconds allow us to “watch” the photoexcitation event and the subsequent coherent dynamics, the coherent-to-incoherent crossover and the slow trend towards the thermalization. We stress that excitonic effects are fully included in the dynamics. In fact, real-time *GW* with

a *statically* screened interaction *W* is equivalent (in linear response) to solving the Bethe-Salpeter equation.^{21,22} Our approach does not rely on effective Hamiltonians written in terms of composite bosons describing excitons; free carriers and excitons both participate to the electronic density matrix. We improve over current real-time *GW* methods in three ways: (i) we use a *dynamically* screened interaction *W*,³⁸ (ii) we account for the interaction with both coherent (Ehrenfest) and incoherent (Fan-Migdal) phonons and (iii) we conserve the total energy of the el-ph system.³⁴ The evolution of the density matrix does therefore embraces the build-up of screening, retardation effects, formation of coherent excitons, and decay into incoherent exciton-polarons (low density)³⁹ or the coherent exciton Mott transition (high density).³⁸

We here put NEGF at work in a molybdenum disulfide (MoS_2) monolayer (Figure 1a) pumped above gap. The direct band gap, tunable in the range 2.0–2.6 eV by varying the substrate,⁴⁰ and the possibility of selectively excite one of the two degenerate valleys with circular polarized light^{41,42} make the MoS_2 monolayer a promising candidate for optoelectronic^{43,44} and valleytronic⁴⁵ applications. Above-gap excitations are relevant for photochemical catalysis, photovoltaic and thermoelectric energy conversion due to the chemical-physical processes triggered by the excess energy of carriers. Our investigation shows that the coherent-to-incoherent crossover is characterized by a dephasing time τ_{deph} which depends on the excitation density n as $\tau_{\text{deph}}^{-1} = \tau_0^{-1} + cn^{1/3}$. The lattice coherence survives much longer than the electronic coherence.⁴⁶ Several hundreds of femtoseconds after the crossover the laser-induced nuclear displacements still oscillate undamped. The dephasing process is accompanied by a highly complex dynamics of carriers and phonons. Intra-valley scattering – mediated by both particle-hole and optical/acoustic phonon emission^{47,48} – is responsible for an ultrafast migration of hot electrons and holes toward the band edges already during pumping, giving rise to spots of different quasi-thermal carrier distributions shortly after the photoex-

citation.⁴⁹ Inter-valley scattering is a slightly slower process, and it is pivotal for reaching a homogeneous thermal distribution across the entire Brillouin zone.⁵⁰ We can distinguish a fast and a slow timescales for the inter-valley scattering. Total energy conservation enables us to shed light on the tangled energy exchange between the electronic and phononic subsystems. We find that the energy gain in the buildup of carrier dressing by phonons is the main responsible for the increase of the lattice temperature during the first 50 – 60 fs. Thereafter the still hot dressed carriers begin to loose their excess energy at a rate of several hundreds of femtoseconds, causing a further increase of the lattice temperature until the end of the thermalization process.

2 Photoexcited dynamics

We study the photoexcited dynamics of a MoS₂ monolayer (Figure 1a) initially at temperature $T = 100$ K driven out of equilibrium by a linearly polarized 15 fs pulse with central frequency ω_0 exceeding the bandgap by 0.2 eV. In our simulations the pump fluence has been varied to span a wide range of excitation densities from 10^{10} up to 10^{14} cm⁻². The excess energy of the hot carriers is released via competing and interconnected processes mediated by both *el-el* and *el-ph* scattering, each one of them having their own timescale. The theoretical analysis of such a complex scenario cannot rely on simplified model Hamiltonians. We therefore solve the NEGF equations of motion for the electronic and phononic density matrices $\rho_{\mathbf{k}ij}$ and $\gamma_{\mathbf{k}\mu\nu}$ (all diagonal and off-diagonal elements are included) using spin-orbit dependent electronic bands $\epsilon_{\mathbf{k}i}$ (Figure 1b-c), with i the spin-band index ($i = v, c$ for valence and conduction respectively) and \mathbf{k} the two-dimensional crystal momentum, phononic bands $\omega_{\mathbf{k}\nu}$, with ν the phonon branch, Coulomb interaction $V_{imjn}^{\mathbf{qkk}'}$ and electron-phonon couplings $g_{\mathbf{k}ik'j}^\nu$ as input^{51,52} (see Note 1 in the Supporting Information for details). The Coulomb integrals responsible for the formation of excitons have the form $V_{cvv'c'}$ and $V_{vc'v'}$, and are explicitly included.

The energy-conserving nature of our approach and the simultaneous inclusion of the time non-local *GW* and *FM* self-energies allows for describing the multiscale dynamics as well as the ultrafast energy exchange between electrons and the underlying lattice.

2.1 Correlation-induced dephasing

The photoexcitation initially generates a hot electron-hole plasma around the K and K' points (Figure 1b-c), more precisely at the conduction and valence energies that approximatively match the condition $\epsilon_{\mathbf{k}c} - \epsilon_{\mathbf{k}v} \simeq \hbar\omega_0$. The plasma inherits the coherence of the laser pulse, as demonstrated by the oscillating macroscopic polarization displayed in Figure 2a. The finite life-time of the polarization is due to interference and dephasing processes. The former are responsible for the so-called “free-induction decay”,⁵³ a phenomenon not related to correlations. As each optical transition oscillates with its own frequency $\epsilon_{\mathbf{k}c} - \epsilon_{\mathbf{k}v}$, the oscillations get rapidly out of phase causing an ultrafast collapse of the macroscopic polarization. The dephasing, instead, destroys the coherence of the electron-hole pairs and convert them into an incoherent admixture of pairs. This process is governed by *el-el* and *el-ph* scattering, and it is distinct from the free-induction decay since all \mathbf{k} -components $P_{\mathbf{k}}(t) = \sum_{cv} \text{Re}[d_{vc\mathbf{k}} \rho_{\mathbf{k}cv}]$, $d_{\mathbf{k}cv}$ being the valence-conduction dipole matrix elements along the polarization direction of the laser (see Note 1 in the Supporting Information), of the macroscopic polarization $P(t) = \sum_{\mathbf{k}} P_{\mathbf{k}}(t)$ damp. In order to assess the correlation-induced dephasing time τ_{deph} we then introduce the more sensible quantity $P_{\text{deph}}(t) = \sum_{\mathbf{k}} |P_{\mathbf{k}}(t)|$. NEGF simulations in a two-band jellium-like model reported a dependence of τ_{deph} on the excited carrier density n ;⁵⁴ in both two-dimensional (2D) and three-dimensional (3D) materials τ_{deph} scales with a power law dependence on the carrier density n according to $\tau_{\text{deph}}^{-1} = \tau_0^{-1} + cn^{1/3}$, where τ_0 is a density-independent contribution due to *el-ph* interactions while the power-law $n^{1/3}$ is an unambiguous signature of the non-Markovian

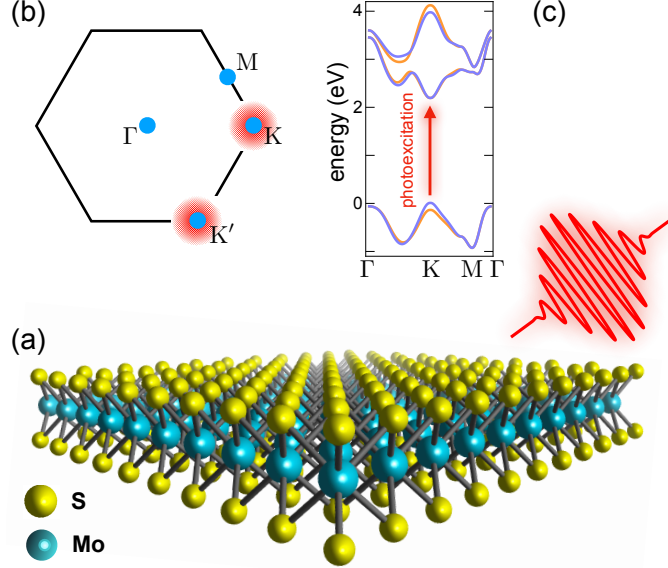


Figure 1: **Coherent-to-incoherent crossover.** (a) Monolayer MoS₂ photoexcited by an ultrafast (15 fs) VIS (516 nm) pulse. (b) First Brillouin zone and the high-symmetry points (blue circles). The VIS pulse excites electrons close to the K point. (c) Band structure including spin-orbit interaction.

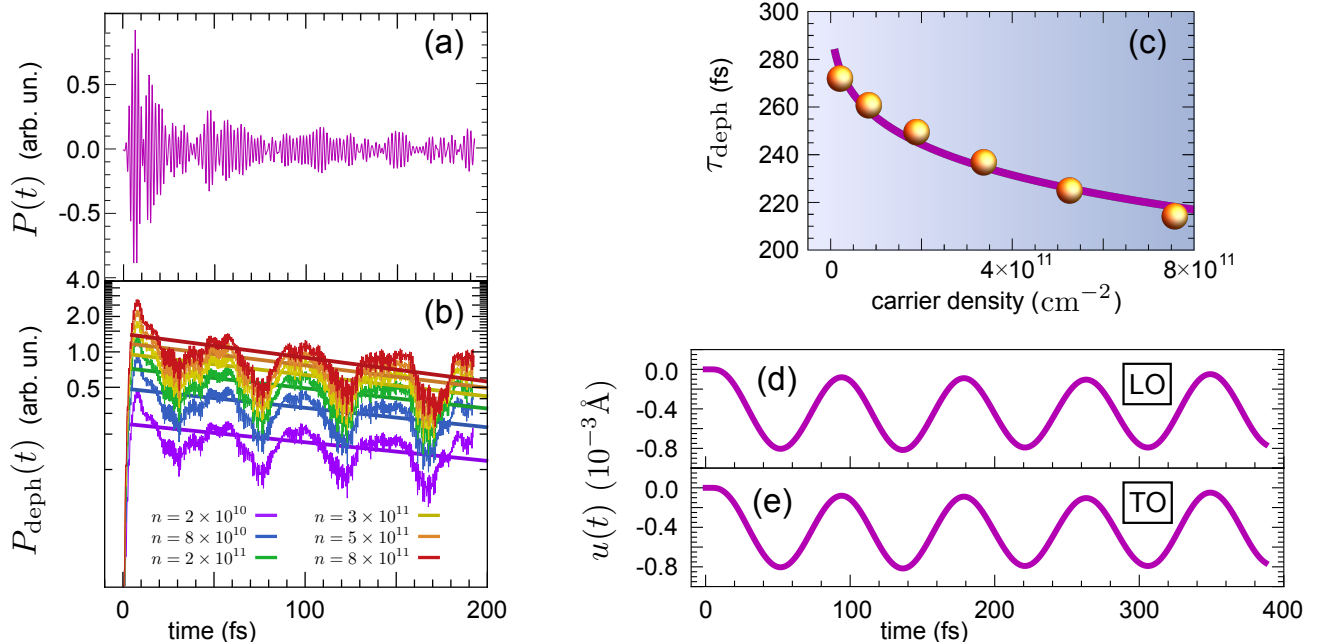


Figure 2: **Coherent-to-incoherent crossover.** (a) Damping of the macroscopic polarization P due to interference and dephasing for carrier density $n = 3 \times 10^{13} \text{ cm}^{-2}$. (b) Logarithmic plot of P_{deph} for different excited carrier densities. (c) Dependence of τ_{deph} on the excited carrier density (circles) and best fit with the function $\tau_{\text{deph}}[n] = \frac{\tau_0}{1 + \tau_0 c n^{1/3}}$. (d-e) Time-dependent nuclear displacement of the LO (top) and TO (bottom) phonons for carrier density $n = 3 \times 10^{13} \text{ cm}^{-2}$. Phonon coherence is preserved during the whole simulations window (~ 400 fs).

quantum kinetics ruled by the *el-el* interaction. This evidence has been experimentally confirmed in 2D and 3D GaAs through measurements of the time-integrated photon echo signal for excitation densities $n \approx 10^{10} - 10^{12} \text{ cm}^{-2}$.⁵⁴

In Figure 2b we display the logarithmic plot of $P_{\text{deph}}(t)$ for different pump fluences, leading to excited carrier densities in the range $10^{10} - 10^{12} \text{ cm}^{-2}$. The fits with the exponential function $e^{-t/\tau_{\text{deph}}}$ are shown as straight lines and demonstrate that the dephasing time decreases with increasing n . The dependence of τ_{deph} on the excited carrier density is explicitly reported in Figure 2c. To verify whether the simulated dynamics is compatible with the universal scenario of Ref.⁵⁴ we best fit our data with the function $\tau_{\text{deph}}[n] = \frac{\tau_0}{1 + \tau_0 c n^{1/3}}$, obtaining the values $\tau_0 = 311 \text{ fs}$ and $c = 1.50 \times 10^{-7} \text{ fs}^{-1} \text{ cm}^{2/3}$. The agreement between the best fit (solid line) and the simulation data-points indicates that the dephasing is indeed driven by a non-Markovian dynamics. For larger excitation densities we find that a single exponential is not sufficient to fit $P_{\text{deph}}(t)$ and that a double exponential is more appropriate (Figure S2). This agrees with experimental findings in a five-layer MoS₂.⁴⁹

The inclusion of the Ehrenfest self-energy gives us access to the time-dependent nuclear displacements $u_\nu(t)$ along the different normal modes. In Figure 2d-e we plot $u_\nu(t)$ for the two most coupled optical phonons, i.e., the transverse optical (TO) and longitudinal optical (LO) phonons. Due to the finite carrier density in the conduction band the nuclei oscillate around a non-equilibrium position with a period T_ν of about 85 fs, in agreement with the corresponding phonon frequency $\omega_{0\nu} = 2\pi/T_\nu$. Contrary to the electronic case the nuclear coherence is very long lived, as no damping is observed during the whole simulation time (about 400 fs). This is consistent with a recent experimental work on a MoS₂ monolayer photoexcited by a ultrashort (< 20 fs) pulse reporting that phonon coherence survives for several picoseconds after the photoexcitation.⁵⁵

2.2 Carrier relaxation

The dynamics of electrons and holes initially photoexcited around the K and K' valleys is extremely rich and the effects of *el-el* and *el-ph* interactions is not simply additive. In Figure 3a-c we provide a comprehensive picture of the energy-momentum resolved carrier dynamics for a relatively high excitation density $n = 3 \times 10^{13} \text{ cm}^{-2}$ during the first 50 fs. Intra-valley scattering and the build-up of the Coulomb screening are the fastest processes taking place,³⁰ influencing the dynamics already during illumination. The intrinsic anisotropy introduced by the linearly polarized pulse (Figure S3) is almost entirely washed out already at time $t = 10$ fs (Figure 3a).

In Figure 3d we show the energy-dependent occupations of electrons $n_e(\epsilon) = \sum_{(c,\mathbf{k}):\epsilon_{c,\mathbf{k}}=\epsilon} n_{c,\mathbf{k}}$ and holes $n_h(\epsilon) = \sum_{(v,\mathbf{k}):\epsilon_{v,\mathbf{k}}=\epsilon} (1 - n_{v,\mathbf{k}})$, where the sums run over all \mathbf{k} and over all conduction and valence bands, and the energy is measured with respect to the conduction band minimum and valence band maximum respectively. Right after pumping the carrier distribution is highly non-thermal, with peaks at the energy satisfying the resonant condition $\epsilon_{\mathbf{k}c} - \epsilon_{\mathbf{k}v} \approx \hbar\omega_0$. Although the energy-dependent occupations reach a Fermi-Dirac distribution within the first 40-50 fs the electronic subsystem has not yet thermalized since degenerate \mathbf{k} -points in the first Brillouin zone are not equally populated, see for instance the K and Γ points in the valence band in Figure 3e. The thermalization takes longer than the dephasing as it is still not reached at the end of our simulation time. The two mechanisms contributing to the thermalization are intra- and inter-valley scattering.

Intra-valley scattering – The intra-valley scattering is responsible for the relaxation of carriers toward the bottom of the band valleys (Figure 3e). We can distinguish two distinct time-scales for the initially photoexcited K points. While the laser pulse is active electrons predominantly lose their excess energy due to inelastic *el-el* collisions, thereby causing an ultrafast increase of the electronic correlation energy, see Figure 4a and 4c. After the

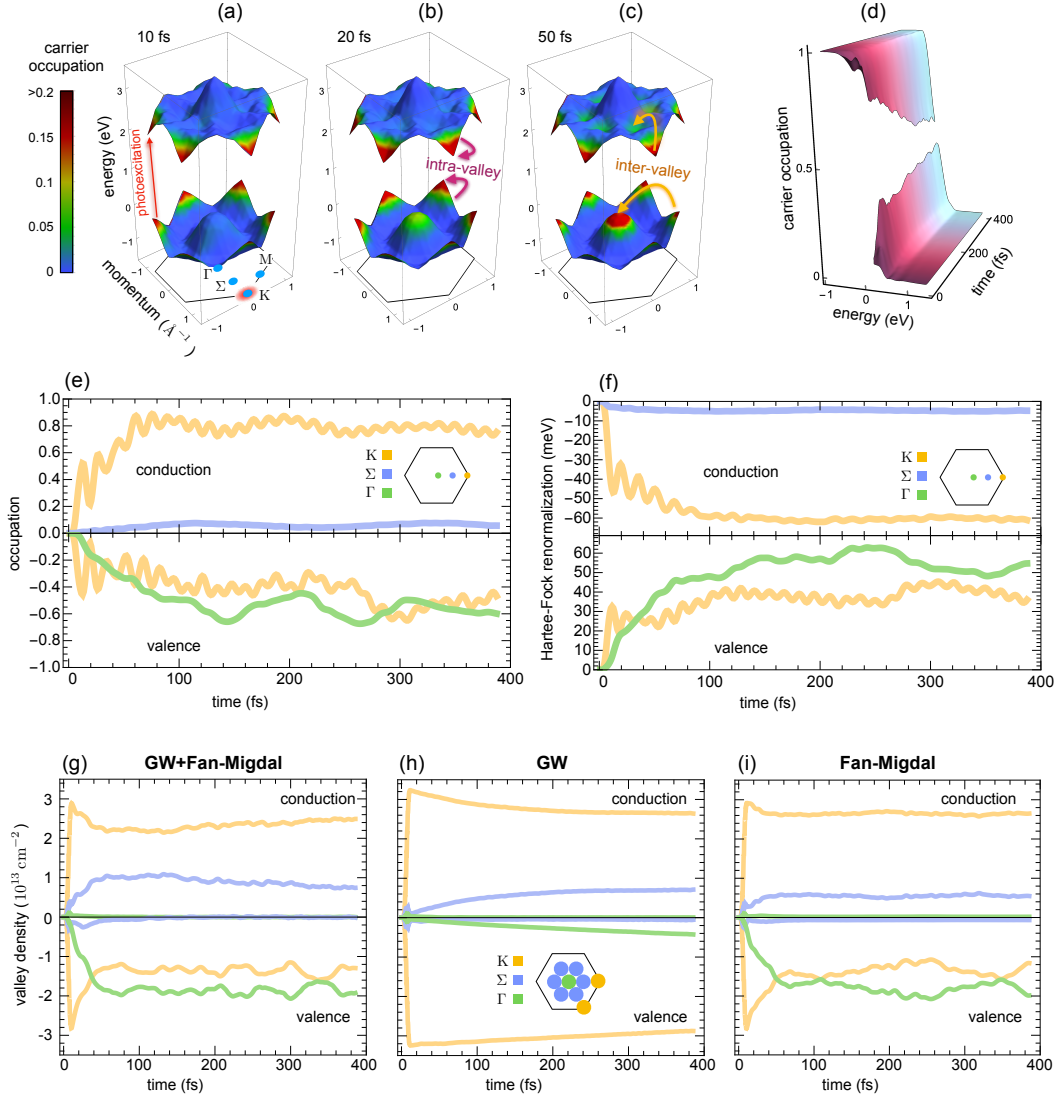


Figure 3: Carrier dynamics (a-c) Snapshots of the \mathbf{k} -resolved electron (for conduction bands) and hole (for valence bands) populations in the first Brillouin zone at times $t = 10$ fs, 20 fs and 30 fs for a MoS₂ monolayer driven out of equilibrium by a laser pump of duration 15 fs and central frequency 0.2 eV larger than the direct gap at the K and K' points. (d) Energy dependent hole populations (for negative energies) and electron populations (for positive energies) as defined in the main text versus time. (e) Time-dependent population at three high-symmetry points of the first Brillouin zone: population of the conduction K point $n_{Kc}(t)$ and Σ point $n_{\Sigma c}(t)$, and valence K point $n_{Kv}(t) - 2$ and Γ point $n_{\Gamma v}(t) - 2$. (f) Time-dependent modification of Hartree-Fock energies at the same high-symmetry points as in panel (e). (g-i) Electronic density in the K and Σ valleys of the conduction band (top) and hole density in the K and Γ valleys of the valence band (bottom) versus time as obtained using NEGF (see Notes 2-3 in the Supporting Information) in the $GW+FM$, GW -only and FM -only approximations. In all panels the carrier density is $n = 3 \times 10^{13} \text{ cm}^{-2}$.

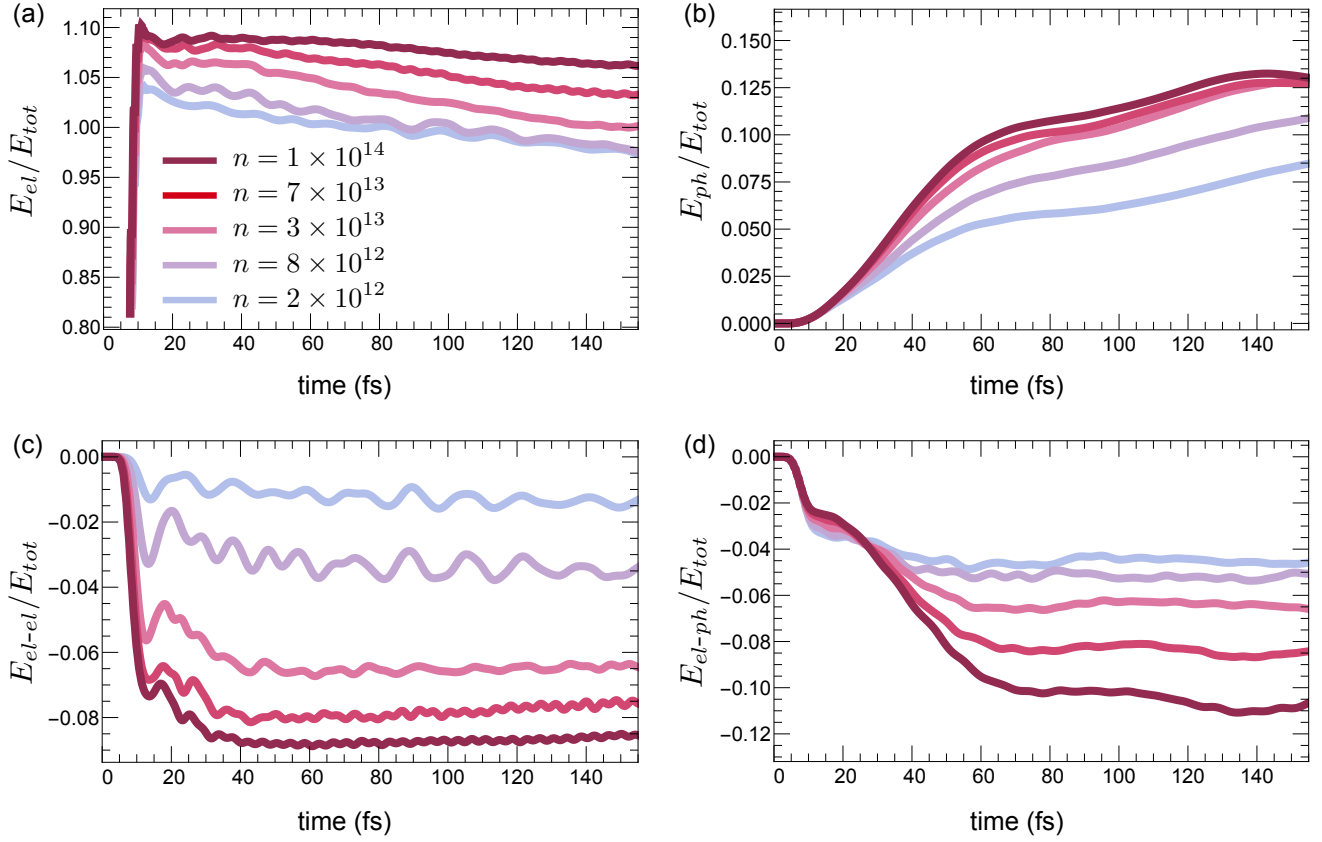


Figure 4: **Energy redistribution** Electronic energy E_{el} [measured with respect to its equilibrium value $E_{el}(t = 0)$] (a), phononic energy E_{ph} (b), $el\text{-}el$ correlation energy E_{el-el} (c) and $el\text{-}ph$ correlation energy E_{el-ph} (d) renormalized to the total energy E_{tot} for different densities of the excited carriers.

photoexcitation intra-valley scattering mainly occurs via the emission of optical and acoustic phonons around the Γ point,^{47,48} the optical contribution being more important than the acoustic one.⁵⁶ The time-scale for reaching a quasi-steady value of the occupations at the K points is about 60 fs (Figure 3e) which is the same time-scale for the initial raise of the phonon energy (Figure 4b). Interestingly, in this time-window the electronic energy is (roughly) constant up to ~ 40 fs (Figure 4a). In fact, the migration toward the bottom of the valley is accompanied by a renormalization of the one-particle energies (Figure 3f). The emission of phonons in this time-window is made possible by the energy gained in dressing electrons and holes with phonons. Such ultrafast process can only be captured with an energy-conserving approach. Inspection of Figure 4b and 4d shows that the rate at which the phonon energy increases is the same as the rate at which the electron-phonon correlation energy (an indicator of phononic dressing) decreases. We also report that holes relax faster than electrons (see flank at positive energy in Figure 3d), in qualitative agreement with recent BE-based simulations.⁵⁰ This is due to the transient trapping of electrons at the bottom of the Σ valley, located about 0.2 eV above the bottom of the K valley.

The electronic correlation energy (Figure 4c) is also an indicator of the *build-up of screening* by the electron-hole plasma. After the pump (15 fs) the correlation energy first decreases (despite the superimposed oscillations) on a time-scale of 40 fs and then begins to increase on a much longer time-scale. This second slower stage of the dynamics is mainly characterized by the equilibration of the populations in different valleys.

Inter-valley scattering – Phonon emission and the build up of screening are concomitant with the second mechanism, i.e., inter-valley scattering. In the first 60 fs an important fraction of excited electrons migrate toward the six degenerate Σ valleys⁵⁷ and an even larger amount of holes migrate towards the Γ valley (Figure 3c and 3g).⁵⁸ In this time-window inter-valley scattering is

mainly a phonon-mediated process, and zone-edge phonons (both optical and acoustic) play a crucial role.^{59–62} This is confirmed by our simulations (see below). Another evidence in favor of the phonon-mediated mechanism is provided in Figure 3i where we include only $el-ph$ scattering through the FM self-energy, and still observe the 60 fs time-scale. Comparing the FM-only dynamics with the GW -only dynamics (Figure 3h) we infer that $el-el$ scattering is much slower in moving electrons between different valleys, although equally important in terms of effectiveness. Inter-valley scattering in GW -only occurs through particle-hole exchange which is initially suppressed by momentum conservation. The full $GW+FM$ dynamics (Figure 3g) reveals an overshooting of charge at the Σ valley of the conduction bands and a rebound of charge between the almost degenerate K and Γ valleys in the valence bands. The near degeneracy of the K and Γ valleys are the cause of the long thermalization time in the MoS₂ monolayer.

Although phonon-exchange and particle-hole exchange live on different time-scales they cannot be treated independently. In fact, the $GW+FM$ dynamics is not merely the FM-only dynamics for times $t < 60$ fs and the GW -only dynamics for $t > 60$ fs (Figure 3e-g). The role of particle-hole exchange diminishes with decreasing the pump fluence. It is only in the regime of weak pumps that the inter-valley FM-only and $GW+FM$ dynamics become similar (not shown).

The four contributions to the total energy (electronic, phononic, electron-electron and electron-phonon) are shown in Figure 4a-d for different densities of the excited carriers. The total energy is correctly constant after the pump (times $t > 15$ fs, not shown). The electronic energy E_{el} remains about ten times larger than the phononic energy E_{ph} whereas the $el-el$ and $el-ph$ correlation energies, E_{el-el} and E_{el-ph} , are comparable in size. We observe that E_{el-ph} saturates after 60 fs (this is the time-scale of the phonon mediated inter-valley scattering) while all other contributions show an almost linear behavior from times $t \sim 60$ fs up to hundreds of femtoseconds (this is the time-scale of the

particle-hole mediated inter-valley scattering).

2.3 Non-equilibrium phonons

The ultrafast photoexcitation of carries promptly activates the dynamics of phonons, whose full density matrix $\gamma_{\mathbf{k}\mu\nu}$ is evolved in time along with the electronic density matrix $\rho_{\mathbf{k}ij}$ and the nuclear displacement u_ν and momentum p_ν of the ν -th mode (see Notes 2-3 in the Supporting Information for details). Through the simultaneous propagation of all these quantities the electronic (phononic) feedback on the phononic (electronic) subsystem is properly accounted for, thereby guaranteeing the conservation of the total energy. The NEGF approach gives us access to several relevant quantities like the mode- and momentum-resolved phonon populations $n_{\mathbf{k}\nu} = \frac{1}{2}(\text{Tr}[\gamma_{\mathbf{k}\nu\nu}] - 1) + \frac{1}{2}\delta_{\mathbf{k},0}(u_\nu^2 + p_\nu^2)$, the mean-squared nuclear displacement $\langle u_\nu^2 \rangle = [\gamma_{0\nu\nu}]_{11}$ and momentum $\langle p_\nu^2 \rangle = [\gamma_{0\nu\nu}]_{22}$ and the *el-ph* correlation energy. The effective temperature of the different phonon modes has been estimated according to $T_{\mathbf{k}\nu} = \hbar\omega_{\mathbf{k}\nu}[k_B \ln(1 + \frac{1}{n_{\mathbf{k}\nu}})]^{-1}$, and the effective (average) lattice temperature according to $T_{av} = \frac{1}{N_{\mathbf{k}}N_{ph}} \sum_{\nu\mathbf{k}} T_{\mathbf{k}\nu}$, where $N_{ph} = 9$ is the total number of phonon branches and $N_{\mathbf{k}}$ is the number of discretized \mathbf{k} -points.

In all our simulations the phonons are initially in thermal equilibrium at a lattice temperature $T = 100$ K. For a wide range of excitation densities the excess energy of hot carriers is transferred to the lattice within the first few hundreds of femtoseconds (Figure 5a), in agreement with recent experiments⁶³ and simulations.⁶⁴ For moderate and high excitation density the energy transfer is characterized by a rapid (within the first 60 fs) increase followed by a slower increase of T_{av} . The final average temperature of 175 K predicted for $n = 10^{14}$ cm⁻² is in excellent agreement with recent BE-based simulations in the same material at the same excitation density.⁵⁰ Although T_{av} is fairly constant after a few hundreds of femtoseconds the \mathbf{k} -dependent temperature remains highly inhomogeneous at this time-scale (Figure 5b). In fact, phonons loose coherence and eventually thermalize on a much longer time-scale than

electrons, see the undamped oscillations of the nuclear displacements in the first 400-fs reported in Figure 2d-e. The energy and momentum constraints of the phonon-assisted energy loss limit the emission of phonons to a few momenta in the first Brillouin zone. We have singled out the emission of optical phonons around the Γ point as a mechanism for intra-valley scattering and the emission of zone-edge acoustic and optical phonons as a mechanism for inter-valley scattering.⁵⁹⁻⁶² It follows that lattice heating is confined around a few high-symmetry points⁵⁰ (Figure 5b), in agreement with recent experiments in MoS₂.⁶⁵ This is a general feature of materials hosting several valleys. Simplified approaches like the two-temperature model are highly questionable in this context, at least during the first few picoseconds. In Figure 5c we show the branch-resolved temperature map for the longitudinal acoustic (LA), transverse acoustic (TA), LO and TO phonons at times $t = 20$ fs and 50 fs. Acoustic phonons are mainly emitted at the Γ point and contribute for about 20% to the overall heating. Optical phonons are mainly emitted at the Γ , K , K' and to a lesser extent at the Σ points, in agreement with the fact that the electronic density in one of the Σ valleys (accompanied by the emission of Σ -phonons) is a factor of ten smaller than the hole density at Γ (accompanied by the emission of K and K' -phonons). The initial raise of the temperature T_ν of the four phonon branches versus time is reported in Figure 5d. We observe a substantial balance between the two optical and the two acoustic modes.

3 Conclusions and outlooks

Atomically thin two-dimensional materials like graphene and the whole family of TMD have broken into the research topics of modern science due to their desirable optoelectronic and valleytronic properties for nanoelectronics, photonics and quantum computing, as well as for their high surface-to-volume ratio for photovoltaic and sensing applications. Time-resolved spectroscopies offer an unprecedented tool to

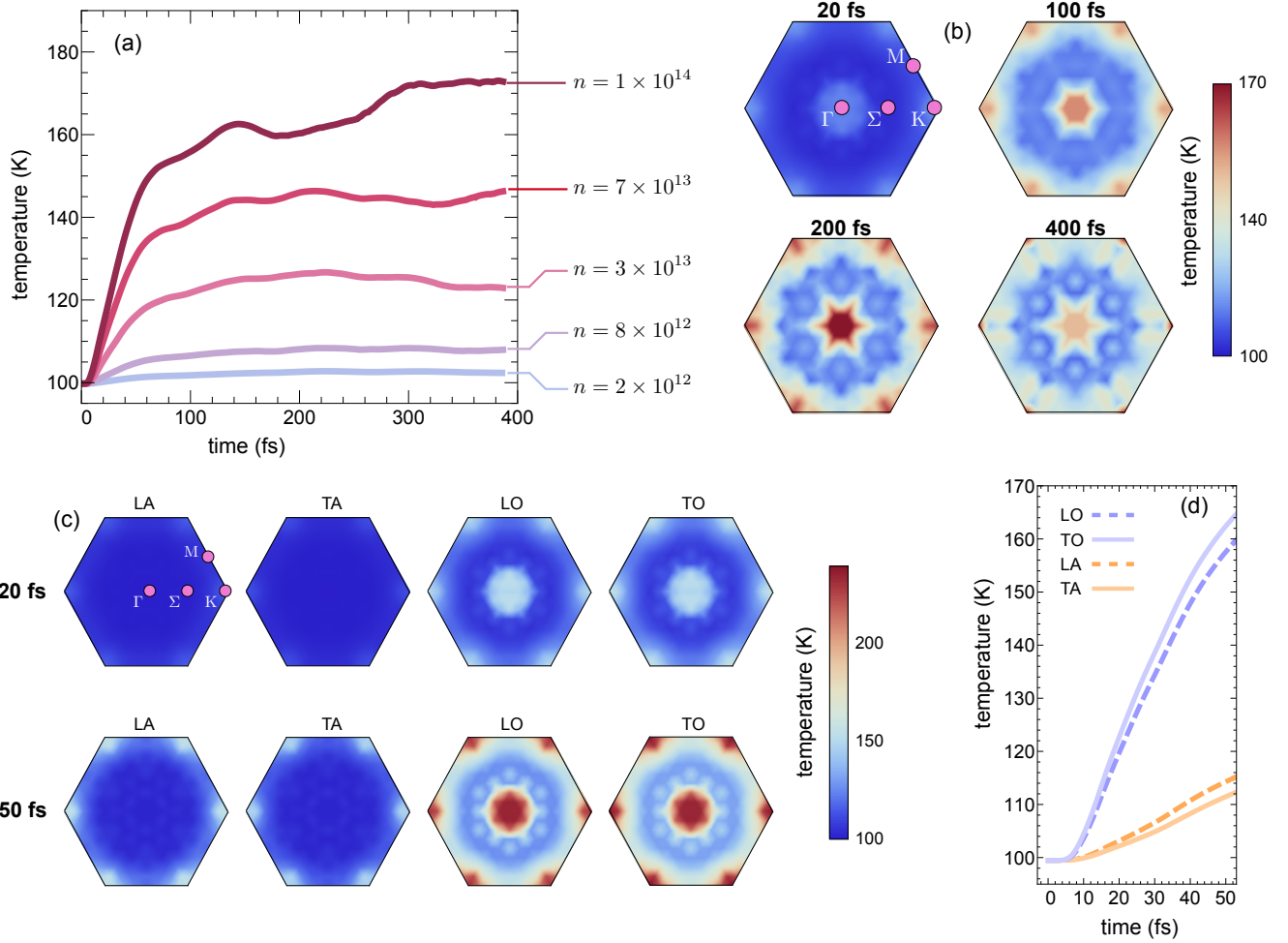


Figure 5: **Phonon Dynamics.** (a) Average temperature versus time for different densities expressed in cm^{-1} . (b) Average temperature map from time $t = 20$ fs to time 400 fs. (c) Branch-resolved temperature maps at times $t = 20$ fs and 50 fs. (d) Branch-resolved temperature for the LA, TA, LO and TO phonons versus time. In panels (b-d) the carrier density is $n = 3 \times 10^{13} \text{ cm}^{-2}$.

characterize these materials and to validate theoretical concepts and techniques indispensable for rationalizing and guiding future research. Developing such techniques is a major challenge due to the simultaneous interplay of light-matter, *el-el* and *el-ph* interactions in an out-of-equilibrium context.

In this work we have presented an advanced ab initio many-body method for real time simulations of 2D systems which encompasses several fundamental aspects, namely the non-Markovian nature of the dynamics for both carrier and polarization degrees of freedom, the electronic feedback on the nuclear degrees of freedom, the effects of nonequilibrium dynamical screening and the conservation of the total energy.

The dynamics of a MoS₂ monolayer pumped above gap has been followed from the instant in which the laser impacts the material until the coherent-to-incoherent crossover and beyond. Agreement with available experimental and theoretical findings on specific aspects of the dynamics has been found. Real-time simulations with/without *el-el* and/or *el-ph* correlations as well as comparisons with Markovian dynamics allows for elucidating the role and the time-scales of entangled physical mechanisms. We point out that many critical processes like the build-up of screening, carrier dressing by phonons, transient lattice heating and intra- and inter-valley scattering occur *during* the coherent-to-incoherent crossover. The resulting scenario is therefore intrinsically complex and hardly interpretable in terms of independent processes.

We foresee a number of further studies and developments. The behavior of different 2D materials optically excited by laser pulses of varying duration, polarization and central frequencies can be characterized through band-, spin- and momentum-resolved carrier populations, polarization, branch- and momentum-resolved phonon populations, electron-electron, electron-hole or exciton, and electron-phonon or polaron correlation functions, nuclear displacements as well as kinetic, potential and correlation energy contributions. The NEGF method can be systematically improved or

adapted to the physical situation of interest. At high pump fluences the dynamical screening of the electron-phonon coupling may become relevant and it can be incorporated through the so called doubly-screened $G\tilde{W}$ approximation³⁵ without affecting the time-scaling. Nonlinear phonon coupling as well as phonon-phonon interactions can be included through the addition of properly chosen self-energy diagrams while preserving the energy conservation law. We add that the time-linear NEGF scheme allows easy parallelisation for high-throughput simulations on denser grids and/or multi-layer systems. We envisage the implementation of the proposed method for parameter-free predictions in (quasi) 2D nonequilibrium materials.

4 Acknowledgements

The Authors acknowledge funding from MIUR PRIN Grant No. 20173B72NB, from INFN17-Nemesys project, Tor Vergata University for financial support through Projects 2DUTOPI and TESLA.

References

- (1) Wang, H.; Zhang, C.; Chan, W.; Tiwari, S.; Rana, F. Ultrafast response of monolayer molybdenum disulfide photodetectors. *Nature Communications* **2015**, *6*, 8831.
- (2) Ma, C.; Wang, C.; Gao, B.; Adams, J.; Wu, G.; Zhang, H. Recent progress in ultrafast lasers based on 2D materials as a saturable absorber. *Applied Physics Reviews* **2019**, *6*, 041304.
- (3) Zhai, X.-P.; Ma, B.; Wang, Q.; Zhang, H.-L. 2D materials towards ultrafast photonic applications. *Phys. Chem. Chem. Phys.* **2020**, *22*, 22140–22156.
- (4) Cheng, J.; Wang, C.; Zou, X.; Liao, L. Recent Advances in Optoelectronic Devices Based on 2D Materials and Their Heterostructures. *Advanced Optical Materials* **2019**, *7*, 1800441.

- (5) Das, S.; Pandey, D.; Thomas, J.; Roy, T. The Role of Graphene and Other 2D Materials in Solar Photovoltaics. *Advanced Materials* **2019**, *31*, 1802722.
- (6) Bettis Homan, S.; Sangwan, V. K.; Balla, I.; Bergeron, H.; Weiss, E. A.; Hersam, M. C. Ultrafast Exciton Dissociation and Long-Lived Charge Separation in a Photovoltaic Pentacene–MoS₂ van der Waals Heterojunction. *Nano Letters* **2017**, *17*, 164–169, PMID: 28073273.
- (7) Li, C.; Cao, Q.; Wang, F.; Xiao, Y.; Li, Y.; Delaunay, J.-J.; Zhu, H. Engineering graphene and TMDs based van der Waals heterostructures for photovoltaic and photoelectrochemical solar energy conversion. *Chem. Soc. Rev.* **2018**, *47*, 4981–5037.
- (8) Sun, X.; Shi, L.; Huang, H.; Song, X.; Ma, T. Surface engineered 2D materials for photocatalysis. *Chem. Commun.* **2020**, *56*, 11000–11013.
- (9) Di, J.; Xiong, J.; Li, H.; Liu, Z. Ultrathin 2D Photocatalysts: Electronic-Structure Tailoring, Hybridization, and Applications. *Advanced Materials* **2018**, *30*, 1704548.
- (10) Li, Y.; Gao, C.; Long, R.; Xiong, Y. Photocatalyst design based on two-dimensional materials. *Materials Today Chemistry* **2019**, *11*, 197–216.
- (11) Mak, K. F.; Shan, J. Photonics and optoelectronics of 2D semiconductor transition metal dichalcogenides. *Nature Photonics* **2016**, *10*, 216–226.
- (12) Tan, C.; Cao, X.; Wu, X.-J.; He, Q.; Yang, J.; Zhang, X.; Chen, J.; Zhao, W.; Han, S.; Nam, G.-H.; Sindoro, M.; Zhang, H. Recent Advances in Ultrathin Two-Dimensional Nanomaterials. *Chemical Reviews* **2017**, *117*, 6225–6331, PMID: 28306244.
- (13) Ceballos, F.; Zhao, H. Ultrafast Laser Spectroscopy of Two-Dimensional Materials Beyond Graphene. *Advanced Functional Materials* **2017**, *27*, 1604509.
- (14) Maiuri, M.; Garavelli, M.; Cerullo, G. Ultrafast Spectroscopy: State of the Art and Open Challenges. *Journal of the American Chemical Society* **2020**, *142*, 3–15, PMID: 31800225.
- (15) Lloyd-Hughes, J. et al. The 2021 ultrafast spectroscopic probes of condensed matter roadmap. *Journal of Physics: Condensed Matter* **2021**, *33*, 353001.
- (16) Burke, K.; Werschnik, J.; Gross, E. K. U. Time-dependent density functional theory: Past, present, and future. *The Journal of Chemical Physics* **2005**, *123*, 062206.
- (17) Miguel AL Marques, F. M. N. E. K. G. A. R., Neepa T Maitra *Fundamentals of time-dependent density functional theory*; Springer Berlin Heidelberg, 2012.
- (18) Maitra, N. T. Perspective: Fundamental aspects of time-dependent density functional theory. *The Journal of Chemical Physics* **2016**, *144*, 220901.
- (19) Tancogne-Dejean, N. et al. Octopus, a computational framework for exploring light-driven phenomena and quantum dynamics in extended and finite systems. *The Journal of Chemical Physics* **2020**, *152*, 124119.
- (20) Yabana, K.; Sugiyama, T.; Shinohara, Y.; Otobe, T.; Bertsch, G. F. Time-dependent density functional theory for strong electromagnetic fields in crystalline solids. *Phys. Rev. B* **2012**, *85*, 045134.
- (21) Attaccalite, C.; Grüning, M.; Marini, A. Real-time approach to the optical properties of solids and nanostructures: Time-dependent Bethe-Salpeter equation. *Phys. Rev. B* **2011**, *84*, 245110.

- (22) Jiang, X.; Zheng, Q.; Lan, Z.; Saidi, W. A.; Ren, X.; Zhao, J. Real-time $\langle i \rangle GW \langle /i \rangle$ -BSE investigations on spin-valley exciton dynamics in monolayer transition metal dichalcogenide. *Science Advances* **2021**, *7*, eabf3759.
- (23) Kadanoff, L. P.; Baym, G. A. *Quantum statistical mechanics: Green's function methods in equilibrium and nonequilibrium problems*; Benjamin, 1962.
- (24) Haug, H.; Jauho, A.-P. *Quantum Kinetics in Transport and Optics of Semiconductors*; Springer: New York, 2008.
- (25) Kira, M.; Koch, S. Many-body correlations and excitonic effects in semiconductor spectroscopy. *Progress in Quantum Electronics* **2006**, *30*, 155–296.
- (26) Haug, H.; Koch, S. W. *Quantum Theory of the Optical and Electronic Properties of Semiconductors*; World Scientific: Singapore, 1994.
- (27) Marini, A. Competition between the electronic and phonon-mediated scattering channels in the out-of-equilibrium carrier dynamics of semiconductors: an ab-initio approach. *Journal of Physics: Conference Series* **2013**, *427*, 012003.
- (28) Steinhoff, A.; Florian, M.; Ršner, M.; Lorke, M.; Wehling, T. O.; Gies, C.; Jahnke, F. Nonequilibrium carrier dynamics in transition metal dichalcogenide semiconductors. *2D Materials* **2016**, *3*, 031006.
- (29) Molina-Sánchez, A.; Sangalli, D.; Wirtz, L.; Marini, A. Ab Initio Calculations of Ultrashort Carrier Dynamics in Two-Dimensional Materials: Valley Depolarization in Single-Layer WSe₂. *Nano Letters* **2017**, *17*, 4549–4555.
- (30) Vu, Q. T.; Haug, H. Time-dependent screening of the carrier-phonon and carrier-carrier interactions in nonequilibrium systems. *Phys. Rev. B* **2000**, *62*, 7179–7185.
- (31) Stefanucci, G.; van Leeuwen, R. *Nonequilibrium Many-Body Theory of Quantum Systems: A Modern Introduction*; Cambridge University Press: Cambridge, 2013.
- (32) Schlünzen, N.; Joost, J.-P.; Bonitz, M. Achieving the Scaling Limit for Nonequilibrium Green Functions Simulations. *Phys. Rev. Lett.* **2020**, *124*, 076601.
- (33) Pavlyukh, Y.; Perfetto, E.; Stefanucci, G. Photoinduced dynamics of organic molecules using nonequilibrium Green's functions with second-Born, GW , T -matrix, and three-particle correlations. *Phys. Rev. B* **2021**, *104*, 035124.
- (34) Pavlyukh, Y.; Perfetto, E.; Karlsson, D.; van Leeuwen, R.; Stefanucci, G. Time-linear scaling nonequilibrium Green's function methods for real-time simulations of interacting electrons and bosons. I. Formalism. *Phys. Rev. B* **2022**, *105*, 125134.
- (35) Pavlyukh, Y.; Perfetto, E.; Stefanucci, G. Interacting electrons and bosons in the doubly screened G W approximation: A time-linear scaling method for first-principles simulations. *Phys. Rev. B* **2022**, *106*, L201408.
- (36) Lipavský, P.; Špička, V.; Velický, B. Generalized Kadanoff-Baym ansatz for deriving quantum transport equations. *Phys. Rev. B* **1986**, *34*, 6933–6942.
- (37) Karlsson, D.; van Leeuwen, R.; Pavlyukh, Y.; Perfetto, E.; Stefanucci, G. Fast Green's Function Method for Ultrafast Electron-Boson Dynamics. *Phys. Rev. Lett.* **2021**, *127*, 036402.
- (38) Perfetto, E.; Pavlyukh, Y.; Stefanucci, G. Real-Time GW : Toward an Ab Initio Description of the Ultrafast Carrier and Exciton Dynamics in Two-Dimensional Materials. *Phys. Rev. Lett.* **2022**, *128*, 016801.
- (39) Stefanucci, G.; Perfetto, E. From carriers and virtual excitons to exciton populations: Insights into time-resolved ARPES

- spectra from an exactly solvable model. *Phys. Rev. B* **2021**, *103*, 245103.
- (40) Naik, M. H.; Jain, M. Substrate screening effects on the quasiparticle band gap and defect charge transition levels in MoS₂. *Phys. Rev. Mater.* **2018**, *2*, 084002.
- (41) Xiao, D.; Liu, G.-B.; Feng, W.; Xu, X.; Yao, W. Coupled Spin and Valley Physics in Monolayers of MoS₂ and Other Group-VI Dichalcogenides. *Phys. Rev. Lett.* **2012**, *108*, 196802.
- (42) Zeng, H.; Dai, J.; Yao, W.; Xiao, D.; Cui, X. Valley polarization in MoS₂ monolayers by optical pumping. *Nature Nanotechnology* **2012**, *7*, 490–493.
- (43) Gupta, D.; Chauhan, V.; Kumar, R. A comprehensive review on synthesis and applications of molybdenum disulfide (MoS₂) material: Past and recent developments. *Inorganic Chemistry Communications* **2020**, *121*, 108200.
- (44) Krishnan, U.; Kaur, M.; Singh, K.; Kumar, M.; Kumar, A. A synoptic review of MoS₂: Synthesis to applications. *Superlattices and Microstructures* **2019**, *128*, 274–297.
- (45) Schaibley, J. R.; Yu, H.; Clark, G.; Rivera, P.; Ross, J. S.; Seyler, K. L.; Yao, W.; Xu, X. Valleytronics in 2D materials. *Nature Reviews Materials* **2016**, *1*, 16055.
- (46) Caruso, F.; Zacharias, M. Quantum theory of light-driven coherent lattice dynamics. *Phys. Rev. B* **2023**, *107*, 054102.
- (47) Nie, Z.; Long, R.; Teguh, J. S.; Huang, C.-C.; Hewak, D. W.; Yeow, E. K. L.; Shen, Z.; Prezhdo, O. V.; Loh, Z.-H. Ultrafast Electron and Hole Relaxation Pathways in Few-Layer MoS₂. *The Journal of Physical Chemistry C* **2015**, *119*, 20698–20708.
- (48) Asakura, E.; Odagawa, T.; Suzuki, M.; Karube, S.; Nitta, J.; Kohda, M. Intravalley scattering probed by excitation energy dependence of valley polarization in monolayer MoS₂. *Journal of Physics D: Applied Physics* **2021**, *54*, 485304.
- (49) Nie, Z.; Long, R.; Sun, L.; Huang, C.-C.; Zhang, J.; Xiong, Q.; Hewak, D. W.; Shen, Z.; Prezhdo, O. V.; Loh, Z.-H. Ultrafast carrier thermalization and cooling dynamics in few-layer MoS₂. *ACS nano* **2014**, *8*, 10931–10940.
- (50) Caruso, F. Nonequilibrium Lattice Dynamics in Monolayer MoS₂. *The Journal of Physical Chemistry Letters* **2021**, *12*, 1734–1740.
- (51) Liu, G.-B.; Shan, W.-Y.; Yao, Y.; Yao, W.; Xiao, D. Three-band tight-binding model for monolayers of group-VIB transition metal dichalcogenides. *Phys. Rev. B* **2013**, *88*, 085433.
- (52) Li, X.; Mullen, J. T.; Jin, Z.; Borysenko, K. M.; Buongiorno Nardelli, M.; Kim, K. W. Intrinsic electrical transport properties of monolayer silicene and MoS₂ from first principles. *Phys. Rev. B* **2013**, *87*, 115418.
- (53) Rossi, F.; Kuhn, T. Theory of ultrafast phenomena in photoexcited semiconductors. *Rev. Mod. Phys.* **2002**, *74*, 895–950.
- (54) Mieck, B.; Haug, H.; Hügel, W. A.; Heinrich, M. F.; Wegener, M. Quantum-kinetic dephasing in resonantly excited semiconductor quantum wells. *Phys. Rev. B* **2000**, *62*, 2686–2695.
- (55) Trovatello, C. et al. Strongly Coupled Coherent Phonons in Single-Layer MoS₂. *ACS Nano* **2020**, *14*, 5700–5710.
- (56) Tong, X.; Bernardi, M. Toward precise simulations of the coupled ultrafast dynamics of electrons and atomic vibrations in materials. *Phys. Rev. Res.* **2021**, *3*, 023072.

- (57) Lee, W.; Lin, Y.; Lu, L.-S.; Chueh, W.-C.; Liu, M.; Li, X.; Chang, W.-H.; Kaindl, R. A.; Shih, C.-K. Time-resolved ARPES Determination of a Quasi-Particle Band Gap and Hot Electron Dynamics in Monolayer MoS₂. *Nano Letters* **2021**, *21*, 7363–7370.
- (58) Xu, S.; Si, C.; Li, Y.; Gu, B.-L.; Duan, W. Valley Depolarization Dynamics in Monolayer Transition-Metal Dichalcogenides: Role of the Satellite Valley. *Nano Letters* **2021**, *21*, 1785–1791.
- (59) Kioseoglou, G.; Hanbicki, A. T.; Currie, M.; Friedman, A. L.; Gunlycke, D.; Jonker, B. T. Valley polarization and intervalley scattering in monolayer MoS₂. *Applied Physics Letters* **2012**, *101*, 221907.
- (60) Jeong, T.-Y.; Bae, S.; Lee, S.-Y.; Jung, S.; Kim, Y.-H.; Yee, K.-J. Valley depolarization in monolayer transition-metal dichalcogenides with zone-corner acoustic phonons. *Nanoscale* **2020**, *12*, 22487–22494.
- (61) Bae, S.; Matsumoto, K.; Raebiger, H.; Shudo, K.-i.; Kim, Y.-H.; Handegard, Ø. S.; Nagao, T.; Kitajima, M.; Sakai, Y.; Zhang, X.; Vajtai, R.; Ajayan, P.; Kono, J.; Takeda, J.; Katayama, I. K-point longitudinal acoustic phonons are responsible for ultrafast intervalley scattering in monolayer MoSe₂. *Nature Communications* **2022**, *13*, 4279.
- (62) Carvalho, B. R.; Wang, Y.; Mignuzzi, S.; Roy, D.; Terrones, M.; Fantini, C.; Crespi, V. H.; Malard, L. M.; Pimenta, M. A. Intervalley scattering by acoustic phonons in two-dimensional MoS₂ revealed by double-resonance Raman spectroscopy. *Nature Communications* **2017**, *8*, 14670.
- (63) He, X.; Chebl, M.; Yang, D.-S. Cross-Examination of Ultrafast Structural, Interfacial, and Carrier Dynamics of Supported Monolayer MoS₂. *Nano Letters* **2020**, *20*, 2026–2033.
- (64) Lin, M.-F. et al. Ultrafast non-radiative dynamics of atomically thin MoSe₂. *Nature Communications* **2017**, *8*, 1745.
- (65) Britt, T. L.; Li, Q.; Renéde Cotret, L. P.; Olsen, N.; Otto, M.; Hassan, S. A.; Zacharias, M.; Caruso, F.; Zhu, X.; Siwick, B. J. Direct View of Phonon Dynamics in Atomically Thin MoS₂. *Nano Letters* **2022**, *22*, 4718–4724.